



Influence of preparation method on zinc oxide properties' for photoelectrochemical application

Meriem Ben Aziza^{1,2} · Yousra Litaïem² · Bernabé Mari Soucase³ · Radhouane Chtourou² · Salah Ammar¹

Received: 13 November 2022 / Revised: 19 August 2023 / Accepted: 22 August 2023
© The Author(s) under exclusive licence to Associação Brasileira de Engenharia Química 2023

Abstract

It is crucial to select an efficient synthesis process, since it is a key factor that significantly influences the efficacy of the synthesized nanomaterials. In this line of thought, the current study provides an insight into the effect of synthesis methods on structural, optical and electrical properties of ZnO thin films. Indeed, this has been achieved by dint of various techniques including: X-ray diffraction (XRD), scanning electron microscope (SEM), energy dispersive X-ray analysis (EDX), contact angle and ultraviolet–visible (UV–Vis) analysis. Equally important, the photoelectrochemical (PEC) performances of the different ZnO films were examined using Linear Sweep Voltammetry technique, Chronoamperometry and Electrochemical Impedance Spectroscopy. Our work illustrates a comparative study of different Zinc Oxide photoanodes prepared by three synthesis's methods: Sol Gel, Hydrothermal and Electrodeposition. It is worth noting that the results from XRD analysis showed that the ZnO photoanodes exhibited a wurtzite phase with a (002) preferential orientation for ZnO (E), ZnO (H) and (101) orientation for ZnO (SG). Besides, the morphological analysis revealed different structures of particles: nanoparticles and nanowires. Additionally, the UV–Vis absorption spectra indicated absorption peaks in the UV region and band gap values of 3.31 eV, 3.07 eV and 3.04 eV were obtained for ZnO (SG), ZnO (H) and ZnO (E) respectively. Among all prepared particles, ZnO nanoparticles elaborated by Sol Gel exhibited a better photocurrent density ($0.072 \text{ mA}\cdot\text{cm}^{-2}$) and the high value of donor density ($5.75 \cdot 10^{21} \text{ cm}^{-3}$). Our work paves the way of potential application of ZnO nanoparticles in water splitting device.

Keywords ZnO · Sol gel · Hydrothermal · Electrodeposition · Photoelectrochemical performances · Water splitting device

✉ Meriem Ben Aziza
benaziameriem52@gmail.com

Yousra Litaïem
yousralitaïem@gmail.com

Bernabé Mari Soucase
bmari@fis.upv.es

Radhouane Chtourou
radhouane.chtourou@gmail.com

Salah Ammar
salah.ammar@fsg.rnu.tn

- ¹ Research Unit of Electrochemistry, Materials and Environment (UREME), Faculty of Sciences of Gabes, University of Gabes, City Erriadh, 6072 Gabes, Tunisia
- ² Laboratory of Nanomaterials and Systems for Renewable Energies (LANSER), Research and Technology Center of Energy, Techno-Park Borj-Cedria, Bp 95, Hammam-Lif, 2050 Tunis, Tunisia
- ³ Institut of Design and Fabrication (IDF), Universitat Politècnica de València, Camí de Vera S/N, 46022 València, Spain

Introduction

ZnO is a promising environment friendly material with a direct band gap of 3.37 eV at room temperature and a high exciton binding energy around 60 meV (Bu and Yeh 2012; Al-Hazmi et al. 2013). Recently, ZnO has been the most utilized metal oxides by researchers because it is easily-manufactured using inexpensive and non-toxic material. These properties mentioned above encourage employing ZnO in numerous photovoltaic devices and optoelectronic, including solar cells, transparent conductive, organic light-emitting diodes (Krunks et al. 2008), photodetector (Mohite and Rajpure 2014), and gas sensor (Paolucci et al. 2021). Furthermore, ZnO is a low-cost material which has long term stability and capability of operating at high temperatures, unlike silicon (Si) based devices which are generally operated at or near room temperature. ZnO is inherently n-type because of the non-stoichiometry created by the presence of native donor

defects, hydrogen defects, oxygen vacancies and/or zinc interstitials (Mahmoud Abdelfataha et al. 2021a; Rokade and 2017a) and it is extremely difficult to obtain p-type ZnO (Qian et al. 2023; Development of Low-Resistance Ohmic Contacts with Bilayer NiO 2023). Many different deposition techniques such as RF-sputtering (Mendil et al. 2019) pulsed laser deposition (PLD) (Vinod Kumar and Ntwaeaborwa 2020), molecular beam epitaxy (MBE) (Li et al. 2023), atomic layer deposition (ALD) (Liu et al. 2013), sol-gel (Dridi et al. 2019; Ben Aziza et al. 2021), thermal oxidation of Zn thin films (Mihailova et al. 2013) and chemical bath deposition (Mahmoud Abdelfataha et al. 2021b), have already been reported. However, in order to realize high-performance ZnO based devices, it is necessary to grow high quality thin films with good crystalline structure on different substrates at low cost. Several previous studies can summarize principal production methods of ZnO thin films and their efficiency for hydrogen production (Table 1) (Liu et al. 2013; Dridi et al. 2019; Ben Aziza et al. 2021; Mahmoud Abdelfataha et al. 2021b; Albadarin et al. 2021; Babu et al. 2015; Karyaoui et al. 2020; Huang et al. 2016; Kant et al. 2018; Rokade et al. 2017b; Lee et al. 2014).

As part of this study, we scrutinize three important and economical ways of fabricating ZnO thin films Hydrothermal (H), Electrodeposition (E) and sol-gel (SG) methods. We study and compare various structural,

optical, and electrical properties of these three kinds of ZnO thin films. Based on characterization studies we demonstrate the quality and further exploratory evidence for potential applications of these structures for water splitting device.

Experimental details

Sample preparation: synthesis of pure ZnO

Pure ZnO thin films were deposited onto indium-doped tin oxide (ITO) glasses. As received commercial ITO thin films from Sigma-Aldrich with surface resistivity near to 8–12 Ω were used as a target material. All chemicals were of analytical reagent grade, purchased from Sigma Aldrich and were used without further purification. Aqueous solutions were prepared using deionized water.

The substrates with dimensions 1 and 0.5 cm were thoroughly cleaned before deposition. The cleaning process was followed by cleaning with ethanol and acetone respectively using an ultrasonic bath for 15 min and finally rinsed with deionized water.

Table 1 Photoelectrochemical performance of different ZnO photoanodes

Preparation method	Substrate	Electrolyte	Light Intensity (mW·cm ⁻²)	Photocurrent Density (mA·cm ⁻²)	References
Atomic layer deposition	ITO	0.1 M KOH	0.5 mW/ cm ²	$I_{cc} = 0.7 \text{ mA}\cdot\text{cm}^{-2}$	Liu et al. (2013)
Sol-gel	ITO-coated glass	0.5 M Na ₂ SO ₄	200 mW/ cm ²	$I_{cc} = 49.3 \mu\text{A}\cdot\text{cm}^{-2}$ $V_{OC} = 0.197 \text{ V}$	Dridi et al. (2019)
Sol Gel	Fluorine doped tin oxide (FTO) substrates	0.5 M Na ₂ SO ₄	200 mW/ cm ²	$I_{cc} = 0.17 \text{ mA}\cdot\text{cm}^{-2}$	Ben Aziza et al. (2021)
Chemical Bath Deposition	ITO-coated glass	0.5 M Na ₂ SO ₄	under AM 1.5	Less than $I_{cc} = 10 \mu\text{A}\cdot\text{cm}^{-2}$	Mahmoud Abdelfataha et al. (2021b)
Hydrothermal	Fluorine doped tin oxide (FTO) substrates	0.5 M Na ₂ SO ₄	100 mW/ cm ²	$I_{cc} = 0.7 \text{ mA}\cdot\text{cm}^{-2}$ at 1.0 V vs Ag/AgCl	Albadarin et al. (2021)
Hydrothermal	SiO ₂ /Si and ITO	0.01 M Na ₂ SO ₄	100 mW/ cm ²	$I_{cc} = 1.46 \text{ mA}\cdot\text{cm}^{-2}$	Babu et al. (2015)
Spray pyrolysis	ITO-coated glass	0.5 M Na ₂ SO ₄	100 mW/ cm ²	$I_{cc} = 0.44 \text{ mA}\cdot\text{cm}^{-2}$ $V_{oc} = 0.38 \text{ V}$	Karyaoui et al. (2020)
Electrodeposition Anodic deposition	Zn foils	0.5 M N Na ₂ SO ₄	100 mW/ cm ²	$I_{cc} = 0.32 \text{ mA}\cdot\text{cm}^{-2}$ at 0.5 V Vs SCE	Huang et al. (2016)
Spray pyrolysis	FTO-coated glass	0.5 M N Na ₂ SO ₄	100 mW/ cm ²	$I_{cc} = 19 \mu\text{A}\cdot\text{cm}^{-2}$	Kant et al. (2018)
Electrodeposition	Fluorine-doped tin oxide (FTO) substrate	NaOH (pH= 11)	100 mW/ cm ²	$I_{cc} = 0.67 \text{ mA}\cdot\text{cm}^{-2}$ at 0.5 Vs SCE	Rokade et al. (2017b)
Sol Gel	F-doped SnO ₂ glass substrates	0.5 M N Na ₂ SO ₄	100 mW/ cm ²	$I_{cc} = 0.28 \text{ mA}\cdot\text{cm}^{-2}$	Lee et al. (2014)

Electrodeposition synthesis

We prepared an aqueous solution containing 5.10^{-4} M ZnCl_2 and 0.1 M KCl under continuous bubbling of oxygen (Riveros et al. 2002). We used an electrodeposition process which involved a classical three-electrode electrochemical cell:

Reference electrode: Ag/AgCl,

Counter electrode: platinum wire.

Working electrode: glass ITO.

The electrodeposition was carried out at fixed potential of -1.0 V versus Ag/AgCl using an Autolab PGSTAT30 potentiostat. The deposition time was 3 h at 80°C (Brayek et al. 2014).

The OH^- ions adsorbed on the glass electrode react with the Zn^{2+} ions coming from the dissociation of ZnCl_2 in water (Eq. 1) to form ZnO nanowires (Pauporte and Lincot 1999).

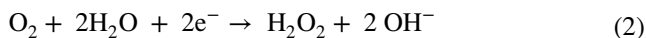
Thus, the synthesis of ZnO nanowires by reduction of molecular oxygen can be carried out according to several steps: (Fig. 1).

a. *Migration*: O_2 molecules migrate towards the cathode by diffusion when the solution becomes saturated with O_2 .

b. *Adsorption*: After migration, the O_2 molecules adsorb on the surface of the electrode on one or two sites (Mustain and Prakash 2007) so that they give rise to reduction mechanisms by exchange of two (Eq. 2) or four (Eq. 3) electrons. The origin of this difference is due to the pH of the solution used and the surface condition of the electrode (Jiang et al. 1991; Strbac and Adžić 1996).

c. *Reduction*: Then, a potential of -1 V vs Ag/AgCl or ECS is applied to ensure the reduction of O_2 into OH^- ions (Eqs. 2 and 3) at the surface of the electrode.

d. *Precipitation*: At the end, the OH^- ions adsorbed on the electrode react with the Zn^{2+} ions (coming from the dissociation of ZnCl_2 in water, Eq. 1) to deposit the ZnO nanowires.



Hydrothermal synthesis

0.01 M of hexamethylenetetramine was added to 0.01 M of zinc nitrate hexahydrate. Then the mixture was transferred to an autoclave in which the ITO substrates were vertically placed. The reactor was heated at 80°C for 24 h. After cooling down at room temperature, the samples were taken out of the autoclave and rinsed with deionized water. Finally, they were calcined at 500°C for 1 h.

Sol Gel synthesis

The zinc oxide thin films were prepared using sol-gel technique spin-coating method. We used the zinc acetate dihydrate as precursor and ethanol as a solvent. The diethylene

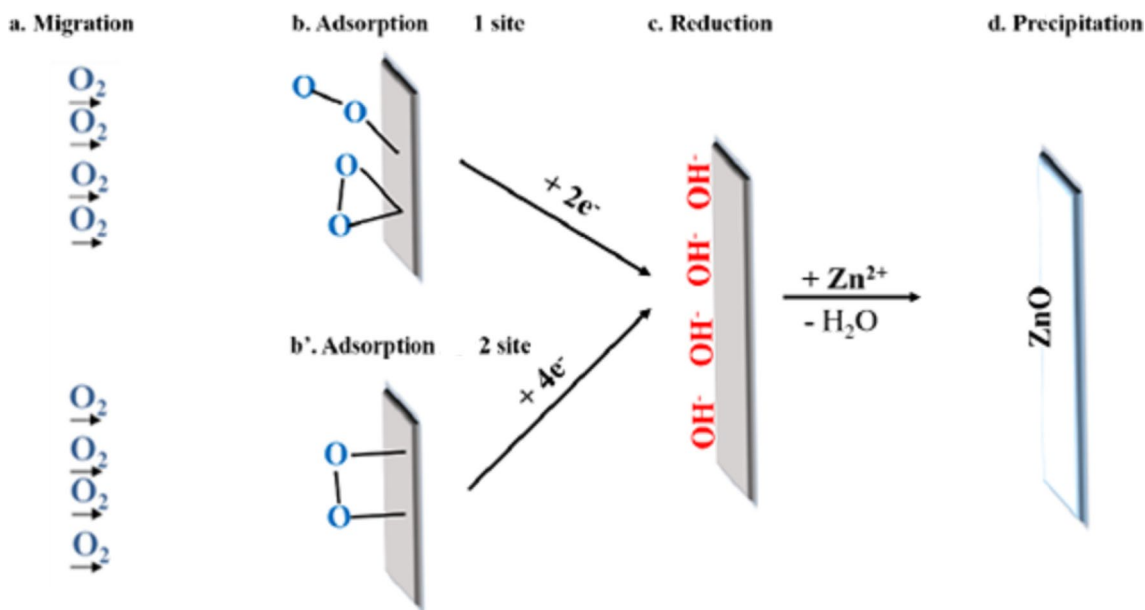


Fig. 1 Steps process for formation of Zinc oxide nanowires

glycol is used as additive. The mixture was stirred by a magnetic stirrer at 60 °C for 6 h until obtaining a clear and homogeneous solution then allowed to age for 48 h Spin coating is done on glass substrate of speed of 3000 rpm for 30 s. After each layer deposition, the spin-coated ZnO/ITO was heat-treated at 100 °C for 10 min to evaporate the solvent and remove organic residual. The processing step was repeated for 6 times to obtain a desired thickness, and finally, all samples were annealed at 500 °C for 1 h in ambient atmosphere (Ben Aziza et al. 2021).

Characterization techniques

Structural characterization of the films was carried out by using X-ray diffraction (XRD) using Bruker D8 advance X-ray diffractometer with Cu K α ($k = 1.541 \text{ \AA}$) radiation for 2θ values in the range of 10–60°. The composition and microstructure of the films were examined using energy dispersive x-ray analysis and scanning electron microscope (FE-SEM) (ZEISS UL TRA55) at acceleration voltage 10 kV. UV–Vis spectroscopy (Lambda 950) was used for the measurement of the optical properties in the wavelength range of 300–800 nm.

To figure out the photoelectrochemical performance measurements of the samples, we used three-electrode arrangement in a quartz electrolytic cell: ZnO thin film as a working electrode, a platinum as a counter electrode, an (Ag/AgCl) as a reference electrode, and a 0.5 M Na₂SO₄ aqueous solution is used as an electrolyte.

All measurements were carried out in air environment at room temperature. Current densities, as a function of

applied potential (−0.6 to +0.5 V vs. Ag/AgCl electrode) for the samples, were recorded under front-side illumination with a computer-controlled Autolab potentiostat metrohm potentiostat/ galvanostat PGSTAT 30. A 300 W Xe short arc lamp (Perkin Elmer Model PE300BF) with white light intensity of 200 mW/cm² was employed to simulate solar light. The intensity of incident light from the Xe lamp was measured using a photometer model 70,310 from Spectra-Physics. The films were examined by linear sweep voltammetry techniques, chronoamperometry, and electrochemical impedance spectroscopy analysis.

Results and discussions

XRD

The X-ray diffraction (XRD) analysis was applied to determine the crystallinity and characteristics of the prepared ZnO thin films.

Figure 2 show the typical XRD patterns of ZnO thin films from different solutions.

The presence of hexagonal ZnO is revealed by the peaks observed at $2\theta = 31.7, 34.4, 36.2, 47.5$ and 56.5 matches up with the lattice planes (100), (002), (101), (102) and (110) respectively.

These results were in agreement with the JCPDS card No. 36–1451 of ZnO wurtzite. A similar outcome has been made by other researchers like Fazel and AL, M. Ashokkumar (Ghahramanifard et al. 2017; Ashokkumar and Muthukumar 2014).

No secondary peaks have been seen, this is reflected by the absence of impurities validating the pure form of ZnO.

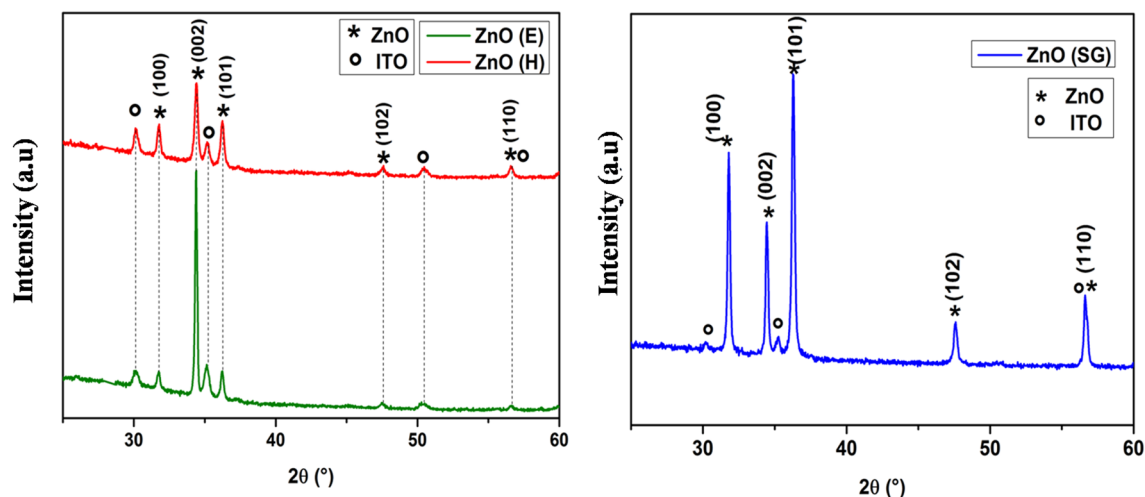


Fig. 2 XRD patterns of ZnO by electrodeposition ZnO (E), hydrothermal method ZnO (H) and Sol Gel method ZnO (SG)

Table 2 crystallite size of different pure ZnO photoanodes

ZnO pur	$\beta_{1/2}$	2θ	D (nm)
ZnO (E)	0.1413	34.3878	102
ZnO (H)	0.2483	34.411	58
ZnO (SG)	0.1968	36.2557	74

Table 3 Thickness of thin films obtained

Pure ZnO	ZnO (E)	ZnO (H)	ZnO (SG)
Thickness (Å)	16,195.58	7902.11	3424.41

According to these results our samples were successfully obtained regardless of the synthesis route used and the precursors were completely decomposed.

From the XRD spectra of samples using hydrothermal (ZnO (H)) and electroplating (ZnO(E)) method, peak (002) is more intense compared to other peaks. Thus growth is preferential along the c axis. Besides, It is observed from Fig. 2 that the XRD peak of (002) plane of ZnO (H) has lower crystallinity than ZnO (E). The widening of peak (002) in ZnO (H) sample can be explained due to the occurrence of defects, lattice-strain and distortion (Rajender and Giri 2016). The lower crystalline quality can be explained due to the occurrence of crystal growth through dissimilar synthesis conditions and the thermal treatment temperature of the samples. The ZnO (H) sample was calcined at 500 °C, which thereby condenses the free O–H groups on the surface of ZnO nanoparticles, lowering the XRD peak intensity of (002) plane (Kaur et al. 2018).

On the other side the sample prepared by the Sol Gel method (ZnO (SG)) has a preferential orientation according to the plan (101).

The average crystallite size D for all samples was calculated by employing the Debye–Scherer formula (Tripathi et al. 2010; Nimbalkar and Patil 2017) as follows:

$$D = \frac{k \times \lambda}{\beta_{1/2} \cdot \cos \theta} \quad (4)$$

where $k=0.90$ is the Scherrer constant (Dehimi et al. 2016; Ali et al. 2015), the Debye-Scherer formula has a shape factor that varies from 0.89 for spherical to 0.94 for cubic particles. Usually, this is set to 0.9 for particles of unknown size, $\beta_{1/2}$ is the width at half maximum and $\lambda=1.5418 \text{ \AA}$ is the wavelength of CuK_α radiation.

The crystallite sizes of ZnO made by different methods have been summarized in the Table 2.

Thus, it is evident that the size differs from one sample to another. The ZnO photoanode prepared by electrodeposition has the largest size (102 nm) while that prepared by hydrothermal was much smaller as compared to other two methods (58 nm).

Morphological analysis

The produced materials were investigated using AFM and SEM to reveal their surface morphology and roughness. The thicknesses of the samples were measured using a Dektak XT Bruker profilometer and the values are presented in Table 3.

Thickness

To produce high quality Zinc oxide photoanodes, films thickness should be studied. This factor can affect the properties of our sample. It was found that the crystalline quality and the grain size increases with film thickness. In our case, ZnO (E) with the biggest average particle size shows a film thickness around 16,195,58 Å much larger than obtained with ZnO (H) and ZnO (SG).

In fact, as reported in the literature, the crystalline quality of the film improves when the film is thicker (Sharma and Mehra 2008; Mridha and Basak 2007).

AFM

The AFM graphs of different ZnO thin films are shown in Fig. 3. These images show that the surface morphologies of the films were strongly dependent on the synthesis methods.

To characterize the surface topography, there are two principal parameters.. The average roughness (Ra) and the root mean square roughness (Rq) (RMS) are the most used amplitude parameters. The last one is more used because this parameter is more sensitive to large deviations with respect to the mean line (Raposo* 2007).

AFM analysis showed that the surface of ZnO (SG) is homogeneous and dense with less root-mean square roughness (RMS) roughness value (113 nm) compared with ZnO (E) and ZnO (H) (see Table 5).

The topography surface of ZnO (E) exhibited agglomeration morphology behavior which is usually obtained for many materials growing by electrodeposition technique with RMS about 240 nm (Kassim et al. 2010).

For ZnO thin films obtained by hydrothermal, the AFM image (Fig. 3.b) revealed that the surface was uniformly covered with small spherical particles with RMS about 216 nm.

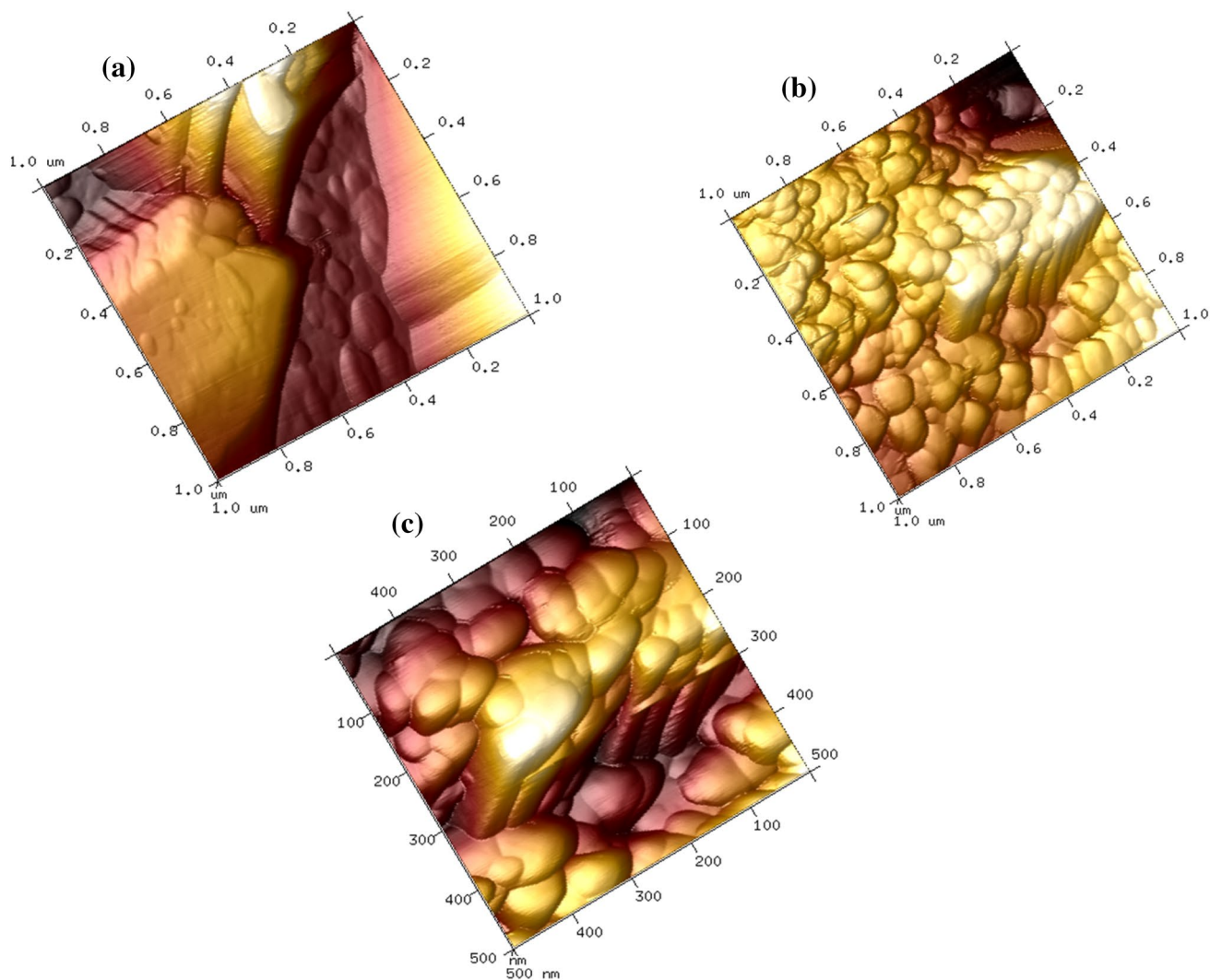


Fig. 3 AFM images of: (a) ZnO(E), (b) ZnO(H), (c) ZnO(SG)

SEM

It was found that the different synthesis's methods lead to the different morphologies of samples as shown from SEM images in Fig. 4.

From Fig. 4a, the structure of zinc oxide hydrothermally synthesized is an agglomeration of groups of spheres which are distanced from each other by a vacuum.

For the SEM image of zinc oxide prepared by electrodeposition Fig. 4b, a dense network of hexagonal ZnO nanowires are aligned evenly and compactly. They grow along the preferred quasi-vertical direction on ITO substrate. Moreover, the diameter of the ZnO nanowires is about 150 nm while their length is in the order of one micrometer.

Figure 4.c reveals the image of zinc oxide prepared by Sol Gel. It shows that the microstructure of this film exhibited

non-uniform grain sizes with mixture of smaller and larger grains. It is a crowding of nanoparticles with different sizes.

In the same figure, the spectra taken by EDX energy dispersive X-ray spectroscopy of the various deposits was used to estimate the chemical composition of the obtained products.

The spectra contain peaks corresponding to Zn and O which confirm the composition of our samples. This is in good agreement with the results obtained by X-ray diffraction.

UV-Vis

According to the absorption spectra of different samples in Fig. 5a, the photoanodes exhibits a strong absorption peak

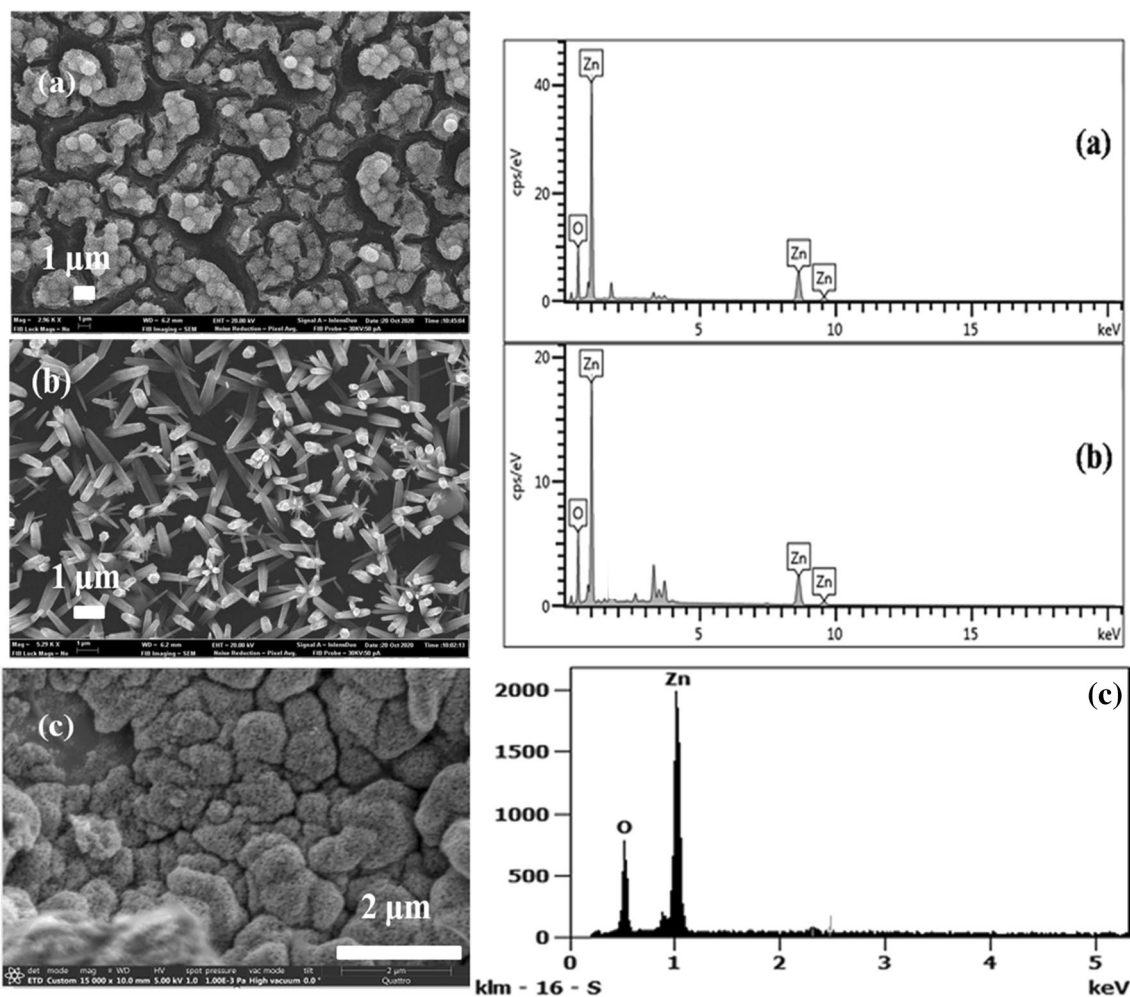


Fig. 4 SEM image of: (a) ZnO(H), (b) ZnO(E), (c) ZnO(SG) and their EDX spectra

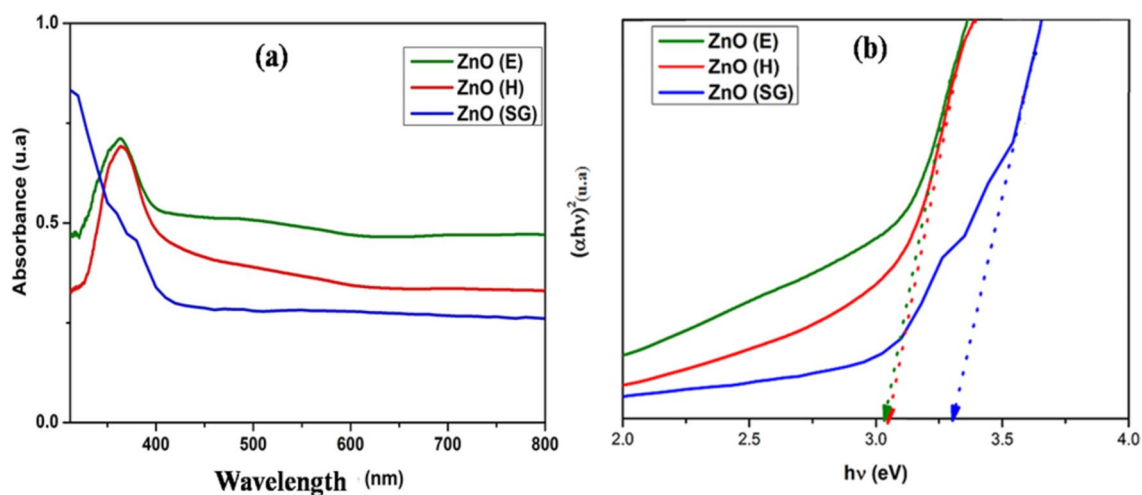


Fig. 5 a UV-vis spectra of pure ZnO, b Plots of $(\alpha h\nu)^2$ versus $(h\nu)$

in the UV region at wavelengths below 400 nm which is in accordance with the absorbance peak for pure ZnO.

The absorbance wavelengths for ZnO (E) and ZnO (H) are very close, around 362 nm and 364 nm respectively, whereas for ZnO (SG), it is around 316 nm.

For a crystalline semiconductor (Zhu et al. 2010), the optical absorption near the edge of the band follows the formula:

$$\alpha h\nu = A(h\nu - E_g)^{n/2} \quad (5)$$

where α is the absorption coefficient, h is Planck constant, ν is the frequency of light, E_g is the band gap and A is a constant, n describes the characteristics of the transition in a semiconductor. For ZnO, the value of n is 1.

The energy band gap (E_g) of films is determined by extrapolating the section of the curve describing the dependence of $(\alpha h\nu)^2$ on the photon energy $h\nu$ for ZnO films with different structures at zero according to the Tauc model. The plot of $(\alpha h\nu)^2$ vs $h\nu$ is based on the direct transition is shown in the following Fig. 5.b.

The value diverges from 3.31 eV \rightarrow 3.07 eV \rightarrow 3.04 eV respectively (Table 4) for the sample ZnO (SG), ZnO (H) and ZnO (E). It can be concluded that the variation of the band gap energy is due to the synthesis methods. Additionally, this behavior can be explained by the increase of film thickness which is noted by many researchers (Landolsi et al. 2018; Khedmi et al. 2014), and the presence of defect level derived from the surface (Ayoub et al. 2022; Ghose, et al. 2019; Park et al. 2020). In general, the band gap in semiconductors is affected by Burstein-Moss effect (Kim et al.

2002), compressive strain (Gaikwad et al. 2014; Rao et al. 2009) and shift in Urbach tail (Sritrakool et al. 1986).

Contact angle

To better understand the wetting characteristics of our samples, we studied the contact angle on the film's surface, which is a very important parameter for photocatalytic applications.

In general, a liquid drop placed on a solid surface forms a noticeable contact angle between solid, liquid and gaseous interfaces. Young proposed theoretical equation relating the interfacial tension to predict the ideal contact angle of absolute smoothness (Young 1805). Later, Wenzel proposed an equation for a real surface by considering the roughness effect on water contact angle (Wenzel 1936). According to Wenzel, the apparent contact angle (θ_w) and the intrinsic contact angle (θ_y) are related by the equation,

$$\cos \theta_w = r_w \cos \theta_y \quad (6)$$

where r_w is the surface roughness factor and is defined as the ratio of intrinsic surface area to its projected surface area. Since, r_w is always greater than 1, therefore increase in roughness enhances the hydrophilicity of hydrophilic ($\theta < 90^\circ$) and the hydrophobicity of hydrophobic ($\theta > 90^\circ$) surfaces.

Figure 6 and Table 5, show the results of the contact angle measurements for water on the different samples.

According to Fig. 6a,b. the samples prepared by hydrothermal method and the electrodeposition show contact

Table 4 Optical band gap of different pure ZnO thin film

Pure ZnO	ZnO (E)	ZnO (H)	ZnO (SG)
E_g (eV)	3.04	3.07	3.31

Table 5 Different values of contact angle and Roughness

Pure ZnO	ZnO (E)	ZnO (H)	ZnO (SG)
Contact Angle ($^\circ$)	124.79	131.6	74.2
R_q	240	250	113
R_a	184	216	94.3

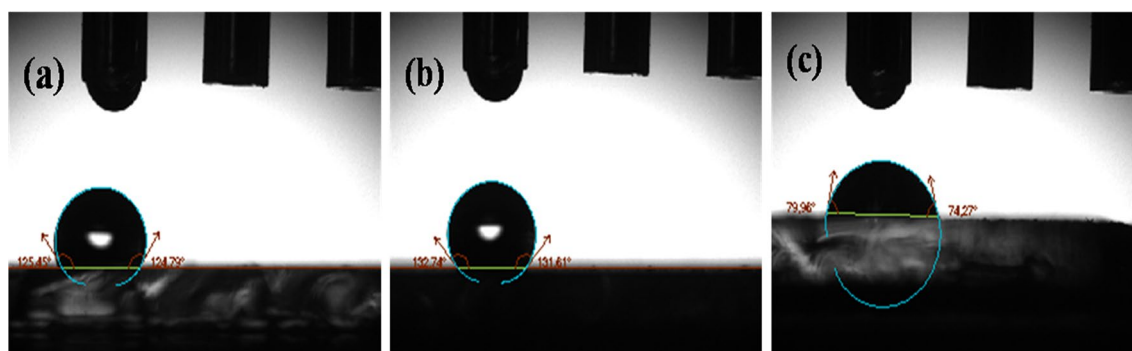


Fig. 6 Contact angle of pure ZnO: (a) ZnO (E), (b) ZnO (H), (c) ZnO (SG)

angle values greater than 90° in the order of 131.6° and 124.79° respectively. The shape of the drops is spherical and flattened by gravity. It can be concluded that the surface is hydrophobic.

For zinc oxide prepared by sol gel method (Fig. 6c), the contact angle value is 74.2° less than 90° . The drop is spread on the surface. The surface of ZnO (SG) is more hydrophilic compared to that of ZnO (E) and ZnO (H). This result may be due to the presence of rich defects in ZnO (SG) compared to the others, in particular the oxygen vacancies which are responsible for the dissociative adsorption of water molecules on the oxide surface, which results in a high hydrophilicity of the zinc oxide surface (Hu et al. 2013).

The influence of surface roughness on the wettability of the films was also investigated.

Surface roughness and contact angle are proportional to each other. The relation between contact angle and surface roughness of ZnO thin films is shown in Table 5. It is observed that the contact angle of ZnO films increases with increase in surface roughness which is consistent with literatures (Khojier et al. 2013; Wang et al. 2010). In addition to that, if the solid surface is hydrophobic (contact angle $> 90^\circ$), the apparent contact angle will increase with the solid surface roughness (Li et al. 2021) which is in good agreement with our result for ZnO (E) and ZnO (H). Their contact angle is about 124.79° and 131.6° respectively and their surface roughness increase from 240 to 250 nm.

PEC

To further verify the above speculation, the transient photocurrent responses and electrochemical impedance spectra (EIS) were measured to examine the charges generation and

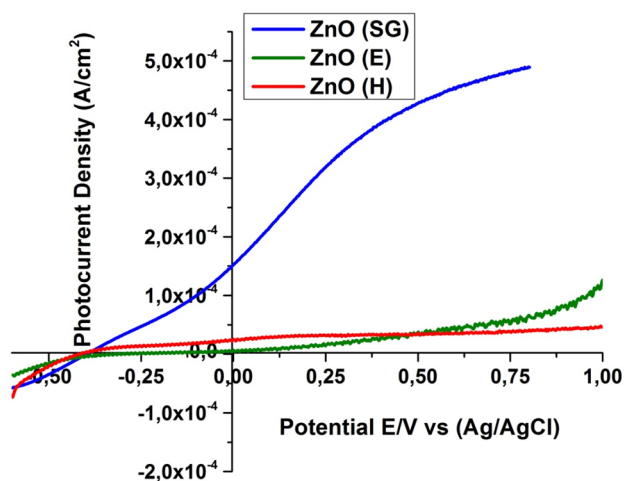


Fig. 7 Linear Sweep Voltammograms of different pure ZnO photoanodes under visible-light irradiation

Table 6 PEC parameters of different samples

	Jsc (mA/cm ²)	Voc (V)
ZnO (E)	0.004	- 0.466
ZnO (H)	0.026	- 0.444
ZnO (SG)	0.072	- 0.414

the transfer behavior in the photoelectrochemistry (PEC) system.

The photoelectrochemical (PEC) properties of the ZnO photoanodes were provided by line-scanning voltammetry (LSV) under irradiation in the potential range of -0.6 to 0.5 V (Fig. 7). The measurements were carried out in the presence of an electrolytic solution of Na_2SO_4 in three-electrode mode under illumination by a Xenon lamp with a power of 200 mW/cm^2 . The photoanode as working electrode, a counter electrode in platinum and a reference electrode in Ag/AgCl.

The following figure shows that the illumination of the working electrode surface by a Xenon lamp causes an increase in current with an increase in the anode potential in the potential range from -0.6 to 0.5 V. Under illumination, all samples have a common behavior: the created photocurrent increases gradually going towards positive potentials which is a characteristic of an n-type conductive semiconductor. The PEC parameters at a fixed bias of 0 V (vs. Ag/AgCl) are listed in Table 6.

The Jsc depends on the number of electrons transferred from the sensitized semiconductor to the conductive substrate, which is also associated with the film area, crystal size, crystal quality and thickness of the nanostructured film (Jie et al. 2014). The Voc depends on the different energy between the edge of the quasi-Fermi band of the photoanode

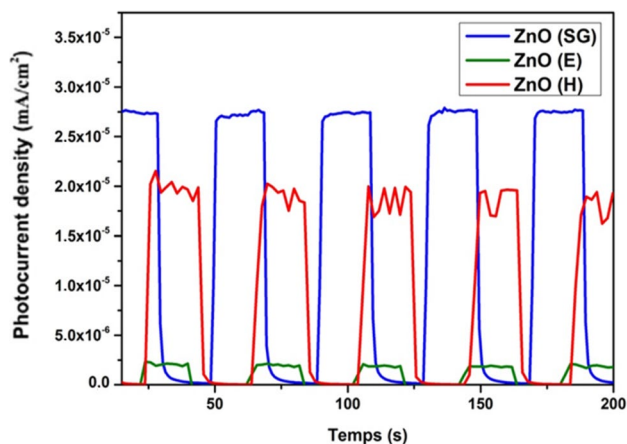


Fig. 8 Photocurrent density response of different pure ZnO thin films as a function of time

and the redox potential of the electrolyte (Zhu et al. 2013). It strongly affects due to electronic recombination between semiconductor/electrolyte interfaces (Wu-Qiang et al. 2013).

The electrical properties of semiconductor nanowires are essential for their realistic use. In fact, the electrical behavior of nanowires is affected by chemical composition, surface properties, size and crystal structure. Nanowires have large surface energy due to their large aspect ratio which increases the imperfections and influences the conductive properties of the material may be this explains the low current density for ZnO (E) photoanode compared to others (Panchal and Chauhan 2019).

To check the stability and the reproducibility of the photo-responses of our photoanodes, we measured the transient photocurrent density in a Na_2SO_4 electrolyte (Fig. 8). This measurement is made for several cycles under alternating lighting at a given potential (0 V) with respect to the Ag/AgCl electrode. We observe in the figure that the photoanodes show an immediate change in photocurrent density upon illumination. On the contrary, as soon as the light is switched off, the photocurrent is retracted towards zero values. The photoanodes remain stable during this operation.

Electrochemical impedance spectroscopy (EIS) is a powerful non-destructive technique to study electron transfer processes at the photoanode/electrolyte interface. The EIS Nyquist curves include the semicircular part at higher frequencies and the linear part at lower frequencies. Part of a semicircle is the charge transfer process whose diameter is equal to the charge transfer resistance.

The Fig. 9a presents the Nyquist curves of the EIS include the semicircular part at higher frequencies, each of Nyquist spectra of the photoanodes made is composed of a semicircle

Table 7 Equivalent circuit parameters

	R_s (Ω)	R_{ct} ($\text{K}\Omega$)	C_{ct} (10^{-6}F)
ZnO (E)	24.5	232	17.1
ZnO (H)	90.3	163	48.8
ZnO (SG)	25.6	104	30.9

at mid-frequency corresponding to the charge transfer resistance at the photoanode/electrolyte interface. The plots revealed an intercept on the real axis (Z') at high frequency which corresponds to the resistance of the solution (R_s). A semicircle in the mid-frequency region corresponds to the charge transfer resistance (R_{ct}) caused by faradic reactions and double layer capacitance (C_{dl}). In fact, the diameter of this semicircle represents the electron transfer resistance of the layer and can be used to describe the interface properties of the electrode. To better understand these variations, the impedance measurements were simulated to electrical circuits using the NOVA impedance measurement processing program. The equivalent electrical circuit is shown in Fig. 9a.

As mentioned in the Table 7 above, the R_s values of different pure ZnO photoanodes are almost constant. While for the charge transfer resistance (R_{ct}) is lower for ZnO (SG) (104 $\text{K}\Omega$) this is in good agreement with the smaller diameter of the half circle corresponds to the ZnO (SG) photoanode presented in the Nyquist curve.

For the different pure zinc oxide photoanodes (Fig. 9b), a single-phase peak is observed in the frequency range of 1–100 Hz. This is consistent with the Nyquist diagram

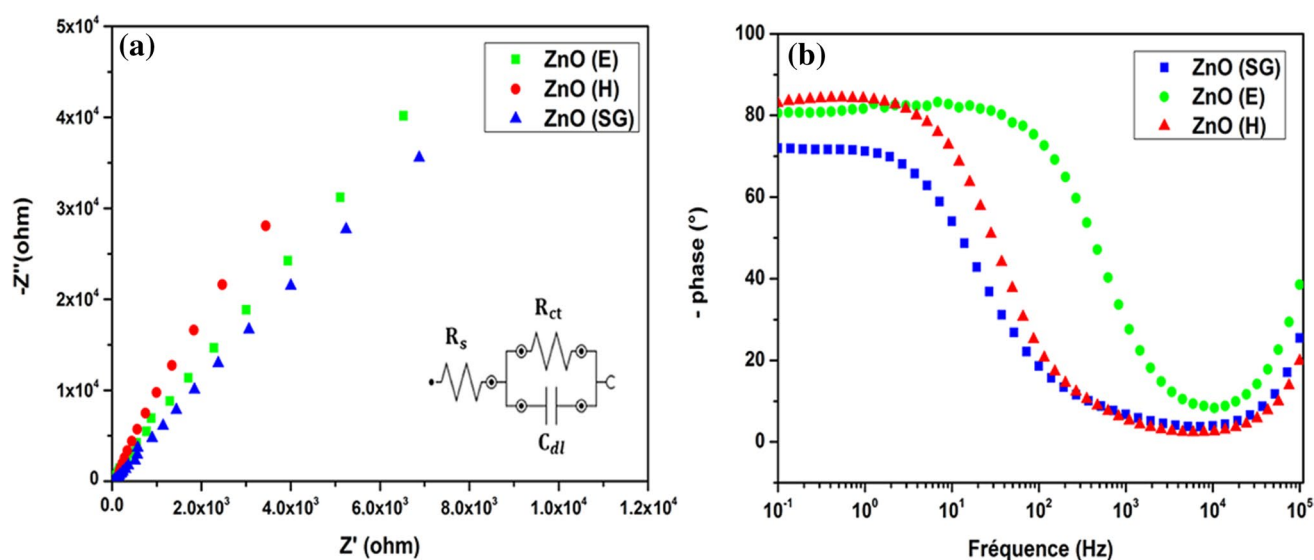


Fig. 9 a Nyquist plots of pure ZnO electrodes immersed in 0.5 Na_2SO_4 electrolyte under dark, b the Phase impedance diagrams

related to the electron transfer process occurring at the electrode/electrolyte interface.

To further testing the effect of each synthesis process on the electronic properties of all ZnO thin films, FRA potential scan measurements have been carried out in dark. It provides information about the intrinsic electronic properties of the semiconductor in contact with the electrolyte solution.

The Mott–Schottky (MS) plots were obtained at 1 kHz to determine the semiconductor type and the value of the flat band potential (V_{fb}) of all obtained samples were estimated using following equation:

$$\frac{1}{C^2} = \frac{2}{eN_D\epsilon_0\epsilon S^2} \left((V - V_{fb}) - \frac{KT}{e} \right) \quad (7)$$

where C is the capacitance of the space charge region, e is the elementary charge of an electron ($e = 1.603 \cdot 10^{-19} \text{C}$), ϵ_0 is the permittivity of vacuum ($\epsilon_0 = 8.854 \cdot 10^{-14} \text{F}\cdot\text{cm}^{-1}$), ϵ is the

Table 8 The values of V_{fb} and the donor densities for ZnO thin films

	ZnO (E)	ZnO (H)	ZnO (SG)
V_{fb} (V)	- 0.75	- 1.24	- 1
N_D (10^{21}cm^{-3})	3.60	4.71	5.75

dielectric constant of the material (in our case = 30) (Zhang et al. 2009), S is the electrochemically active surface area (1cm^2), V is the applied voltage, V_{fb} is the flat band potential (V), K the Boltzmann constant ($1.381 \cdot 10^{-23} \text{J/K}$) and T the absolute Temperature and N_D stands for the density of donor in the semiconductor (cm^{-3}).

The conductivity type of the semiconductor is indicated by the shape of Mott-schottky plot, the p-type will

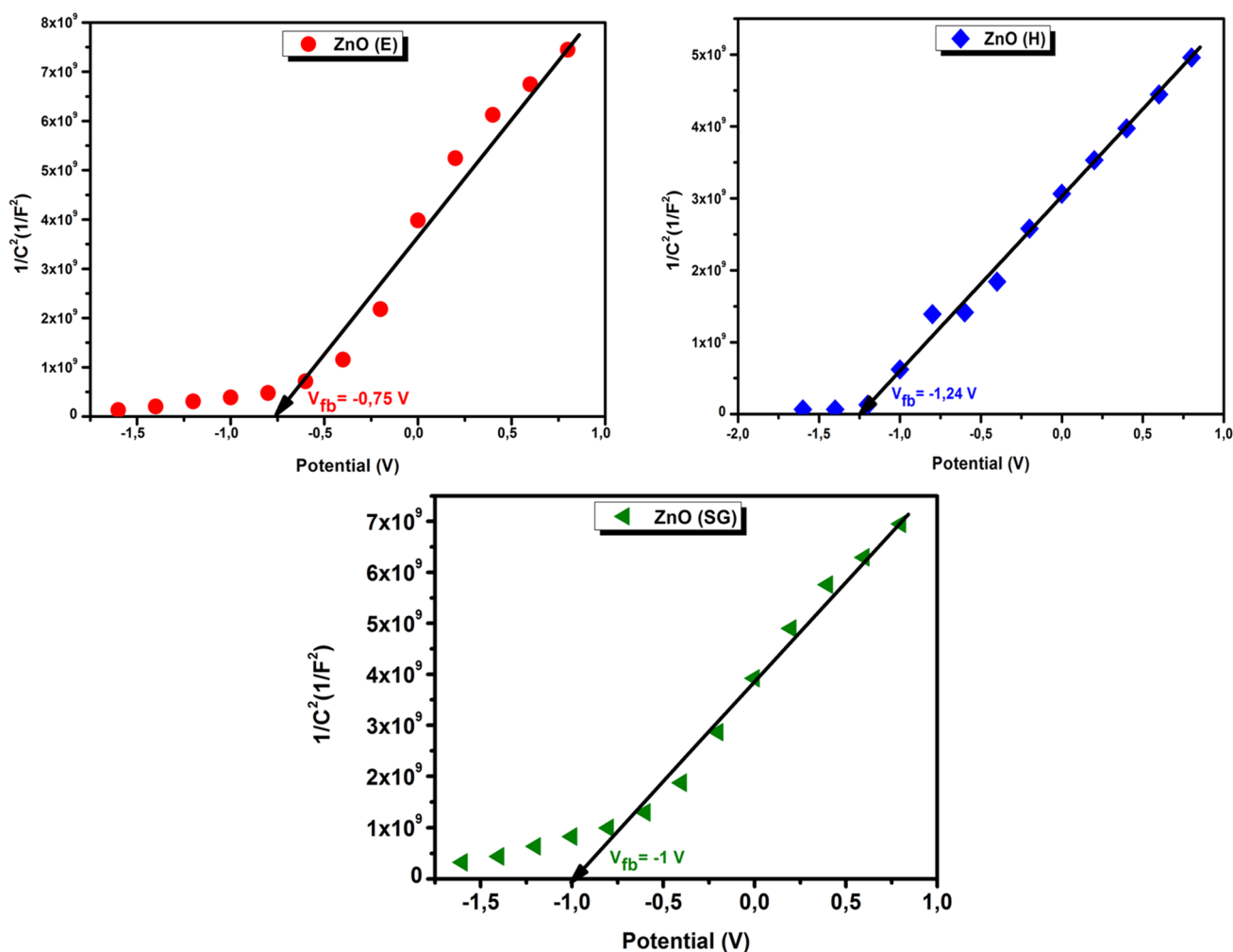


Fig. 10 Mott-Schottky plots of different ZnO thin films using different elaboration process in the dark at frequency of 1 kHz

be indicated by a negative slope and the positive one corresponds to n-type semiconductor.

The Mott-schottky (M-S) plots for all different ZnO photoanodes obtained shown in Fig. 10. We noted that all (M-S) of samples illustrate positive slopes, indicating n-type semiconductor. Additionally, the plots are extrapolated to $1/C^2 = 0$ in order to estimate the values of V_{fb} of the different ZnO photoanodes. The estimated flat bands potential were grouped in the Table 8.

This result may be attributed to the differences in crystalline nature of the ZnO particles.

The charge carrier density N_D can be calculated by the following equation (Wu et al. 2014):

$$N_D = \frac{2}{\epsilon \epsilon_0 e_0} \left[\frac{d\left(\frac{1}{C^2}\right)}{dV} \right]^{-1} \quad (8)$$

The carrier donor concentrations (ND) were than calculated and grouped in the Table 8.

We disclose that ZnO thin film elaborated with Sol Gel possess the highest donor density. Such results indicate that the charge transport in this sample will be faster than that in the other films.

Conclusion

We have succeeded in producing zinc oxide by three different synthesis methods: Hydrothermal, Sol Gel and Electrodeposition. All the samples crystallize according to the wurtzite structure with a preferential orientation along (101) for the ZnO photoanode (SG) and along (002) for the other samples of zinc oxide prepared by hydrothermal and electrodeposition. The absorption peaks in the UV region obtained from the UV-Vis absorption spectra of different ZnO thin films were attributed to the band gap of ZnO. We obtain a photoanode behavior by generating a non-zero current under illumination with higher photocurrent density for the zinc oxide photoanode prepared by the sol gel method. This is in good agreement with the result achieved by EIS measurements which is modeled by an equivalent circuit.

The obtained nanostructures can be used in different photocatalytic applications including photoelectrochemical water splitting and solar cells.

Future investigations will focus on the stabilization of these photoanodes. The work is currently in progress and the results will be reported subsequently.

References

- Al-Hazmi F, Aal NA, Al-Ghamdi AA, Alnowaiser F, Gafer ZH, Al-Sehemi AG (2013) Facile green synthesis, optical and photocatalytic properties of zinc oxide nanosheets via microwave assisted hydrothermal technique. *J Electroceramics* 31:324–330
- Ali SM, Farooq WA, Baig MR, Shar MA, Atif M, Alghamdi SS, Algarawi MS, Ur-Rehman N, Aziz MH (2015) Structural and optical properties of pure and Ag doped ZnO thin films obtained by sol gel spin coating technique. *J Mater Sci Pol* 33:601
- Ashokkumar M, Muthukumaran S (2014) Microstructure, optical and FT-IR studies of Ni, Cu codoped ZnO nanoparticles by co-precipitation method. *Opt Mater* 37:671–678
- Avinash R, Sachin R, Vidhika S, Mohit P, Habib P, Sandesh J (2017a) Electrochemical synthesis of 1D ZnO nanoarchitectures and their role in efficient photoelectrochemical splitting of water. *J Solid State Electrochem* 21:2639–2648
- Avinash R, Sachin R, Vidhika S, Mohit P, Habib P, Sandesh J (2017b) Electrochemical synthesis of 1D ZnO nanoarchitectures and their role in efficient photoelectrochemical splitting of water. *J Solid State Electrochem* 21:2639–2648
- Ayoub I et al (2022) Advances in ZnO: manipulation of defects for enhancing their technological potentials. *Nanotechnol Rev* 11:575–619
- Babu ES, Hong SK, Vo TS et al (2015) Photoelectrochemical water splitting properties of hydrothermally-grown ZnO nanorods with controlled diameters. *Electron Mater Lett* 11:65–72
- Ben Aziza M, Litaïem Y, Chtourou R, Ammar S (2021) The influence of different stabilizers on properties of sol-gel spin coated zinc oxide films. *Braz J Phys*
- Brayek A, Ghoul M, Soussi A, Ben assaker I, Lecoq H, Nowak S, Chaguetmi S, Ammar S, Oueslati M, Chtourou R (2014) Synthesis of core/shell ZnO/ZnSe nanowires using novel low cost. *Mat Lett* 129:142–145
- Bu IY, Yeh YM (2012) Effects of sulfidation on the optoelectronic properties of hydrothermally synthesized ZnO nanowires *Ceramics International* 38:3869–3873
- Dehimi M, Touam T, Chelouche A, Boudjouan F, Bouasla A, Djouadi D, Fischer A, Boudrioua A, Doghmane A (2016) Influence of low Ag doping on structural, morphological and optical properties of sol-gel dip-coated nanostructured ZNO thin films. *Int J Nat Sci Res* 4:2311
- Dridi D, Litaïem Y, Karyouli M, Chtourou R (2019) Correlation between photoelectrochemical and photoluminescence measurements of Ag-doped ZnO/ITO photoanode. *Eur Phys J Appl Phys* 85:20401
- Fazel G, Omid F, Ahmad R (2017) Electrodeposition of Cu-doped p-type ZnO nanorods; effect of Cu doping on structural, optical and photoelectrocatalytic property of ZnO nanostructure. *Superlattices Microstruct*
- Gaikwad SS, Gandhi AC, Pandit SD, Pant J, Chan T-S, Cheng C-L, Ma Y-R, Wu SY (2014) Oxygen induced strained ZnO nanoparticles: an investigation of Raman scattering and visible photoluminescence. *J Mater Chem c* 2:7264–7274
- Hu H, Ji H-F, Sun Y (2013) The effect of oxygen vacancies on water wettability of a ZnO surface. *Phys Chem Chem Phys* 15:16557
- Jiang S, Cui C, Tseung A (1991) Reactive seposition of cobalt electrodes V. Mechanistic studies of oxygen reduction in unbuffered neutral solutions saturated with oxygen, *Electrochem Soc* 138(12):3599–3605

- Jie Qu, Yang Y, Qingduan Wu, Coxon PR, Liu Y, He X, Xi K, Yuan N, Ding J (2014) Influence of solution viscosity on hydrothermally grown ZnO thin films for DSSC applications. *RSC Adv* 4:11430
- Kant R, Dwivedi C, Pathak S, Dutta V (2018) Fabrication of ZnO nanostructures using Al doped ZnO (AZO) templates for application in photoelectrochemical water splitting. *Appl Surf Sci* 447:200–212
- Karyaoui M, Ben Jemia D, Gannounia M, Ben Assakera I, Bardaouia A, Amloukb M, Chtourou R (2020) Characterization of Ag-doped ZnO thin films by spray pyrolysis and its using in enhanced photoelectrochemical performances. *Inorganic Chem Commun* 119:108114
- Kassim A, Nagalingam S, Min HS, Karrim N (2010) XRD and AFM studies of ZnS thin films produced by electrodeposition method. *Arab J Chem* 3:243–249
- Kaur G, Negi P, Kaur M et al (2018) Morpho-structural and optoelectrical properties of chemically tuned nanostructured TiO₂. *Ceram Int* 44(15):18484–18490
- Khedmi N, Rabeh MB, Kanzari M (2014) Structural morphological and optical properties of SnSb₂S₄ thin films grown by vacuum evaporation method. *J Mater Sci Technol* 30:1006–1011
- Khojier K, Savaloni H, Shokrai E, Dehghani Z, Dehnavi NZ (2013) Influence of argon gas flow on mechanical and electrical properties of sputtered titanium nitride thin films. *J Theor Appl Phys* 7(1):1
- Kim H, Horwitz J, Qadri S, Chrisey D (2002) Epitaxial growth of Al-doped ZnO thin films grown by pulsed laser deposition. *Thin Solid Films* 420–421:107–111
- Krunks M, Katerski A, Dedova T, Oja Acik I, Mere A (2008) Nanostructured solar cell based on spray pyrolysis deposited ZnO nanorod array. *Sol Energy Mater Sol Cells* 92:1016–1019
- Landolsi Z, Assaker IB, Chtourou R, Ammar S (2018) Photoelectrochemical impedance spectroscopy of electrodeposited hematite a-Fe₂O₃ thin films: effect of cycle numbers. *J Mater Sci Mater Electron* 29:8176–8187
- Lee M-I, Huang M-C, Legrand D, Lerondel G, Lin J-C (2014) Structure and characterization of Sn, Al co-doped zinc oxide thin films prepared by sol-gel dip-coating process. *Thin Solid Films* 570:516–526
- Li C, Zhang J, Han J, Yao B (2021) A numerical solution to the effects of surface roughness on water-coal contact angle. *Sci Rep* 11:459
- Li Qa, Yuan MM, Zhang MD, Guo CG, Liao B, Zhang X, Ying MJ (2023) Effects of Sm implantation on the structure and magnetic properties of polar ZnO films. *J Alloys Compounds*
- Liu M, Nam C-Y, Black CT, Kamcev J, Zhang L (2013) Enhancing water splitting activity and chemical stability of zinc oxide nanowire photoanodes with ultrathin titania shells. *J Phys Chem C* 117(26):13396–13402
- Mao-Chia H, TsingHai W, Bin-Jui W, Jing-Chie L, Ching-Chen W (2016) Anodized ZnO nanostructures for photoelectrochemical water splitting. *Appl Surface Sci* 360(Part B):442–450
- Mahmoud A, Salaha HY, EL-Henaweyc MI, Orabyc AH, Abdelhamid E-S, Walid I (2021a) Insight into Co concentrations effect on the structural, optical, and photoelectrochemical properties of ZnO rod arrays for optoelectronic applications. *J Alloys Compounds* 873(25):159875
- Mahmoud A, Salaha HY, EL-Henaweyc MI, Orabyc AH, Abdelhamid E-S, Walid I (2021b) Insight into Co concentrations effect on the structural, optical, and photoelectrochemical properties of ZnO rod arrays for optoelectronic applications. *J Alloys Compounds* 873(25):159875
- Mendil D, Challali F, Touam T, Chelouche A, Souici AH, Ouhenia S, Djouadi D (2019) Influence of growth time and substrate type on the microstructure and luminescence properties of ZnO thin films deposited by RF sputtering. *J Luminesci* 215:116631
- Mihailova I, Gerbreder V, Tamanis E, Sledevskis E, Viter R, Sarajevs P (2013) Synthesis of ZnO nanoneedles by thermal oxidation of Zn thin films. *J Non-Cryst Solids* 377:212–216
- Mohite SV, Rajpure KY (2014) Synthesis and characterization of Sb doped ZnO thin films for photodetector application. *Opt Mater* 36(4):833–838
- Mridha S, Basak D (2007) Effect of thickness on the structural, electrical and optical properties of ZnO films. *Mater Res Bull* 42:875–882
- Mustain WE, Prakash J (2007) A model for the electroreduction of molecular oxygen. *Electrochem Soc* 154(7):A668–A676
- Nusayba AA, Mohd ST, Mohd NIS, Wong WY, Sin T, Abdul AHK, Lorna JM, Aymen A, Eman S (2021) Hydrothermal synthesis of Ag-ZnO nanostructures as an advanced material for photoelectrochemical applications. *Int J Electrochem Sci* 16:210848
- Nimbalkar AR, Patil MG (2017) Synthesis of highly selective and sensitive Cu-doped ZnO thin film sensor for detection of H₂S gas. *Mater Sci Semicond Process* 71:332–341
- Panchal S, Chauhan RP (2019) Variation in structural, electrical and optical properties of selenium nanowires after irradiation with Ni⁶⁰ ions. *Electron Mater Lett* 15:216–226
- Paolucci V, De Santis, Lozzi L, Rigon M, Martucci A, Cantalini C (2021) ZnO thin films containing aliovalent ions for NO₂ gas sensor activated by visible light. *Ceramics Int* 47(17):25017–25028
- Park J et al (2020) Electrical defect state distribution in single crystal ZnO schottky barrier diodes. *Coatings* 10:206
- Pauporte T, Lincot D (1999) Heteroepitaxial electrodeposition of zinc oxide films on gallium nitride. *Appl Phys Lett* 75(24):3817–3819
- Qian L, Minju Y, Zhongwei L, Lizhen Y, Qiang C (2023) Plasma Sci Technol 23:095503
- Rajender G, Giri PK (2016) Strain induced phase formation, microstructural evolution and bandgap narrowing in strained TiO₂ nanocrystals grown by ball milling. *Jalloys Compd* 676:591–600
- Rao TP, Kumar MCS, Angayarkanni SA, Ashok M (2009) Effect of stress on optical band gap of ZnO thin films with substrate temperature by spray pyrolysis. *J Alloys Compd* 485:413–417
- Raposo* M, Ferreira Q, Ribeiro PA (2007) A guide for atomic force microscopy analysis of soft- condensed matter modern, research and educational topics in microscopy. A Méndez-Vilas and J. Díaz (Eds.)
- Riveros G, Guillemoles JF, Lincot D, Meier HG, Froment M, Bernard MC, Cortes R (2002) Electrodeposition of epitaxial ZnSe films on InP and GaAs from an aqueous zinc sulfate-selenosulfate solution. *Adv Mat* 14:18
- Srabantika G et al. (2019) Defect dependent inverted shift of band structure for ZnO nanoparticles. *Mater Res Exp* 6:105907
- Sharma M, Mehra RM (2008) Effect of thickness on structural, electrical, optical and magnetic properties of Co and Al doped ZnO films deposited by sol-gel route. *Appl Surf Sci* 255:2527–2532
- Sritrakool W, Sa-Yakanit V, Glyde HR (1986) Band tails in disordered systems. *Phys Rev B* 33:1199–1202
- Strbac S, Adžić R (1996) The influence of pH on reaction pathways for O₂ reduction on the Au (100) face. *Electrochim Acta* 41(18):2903–2908
- Taoufik ST*, Clément M, Micka B, Meiling Z, Matthew C, Romain G, Arnaud, Daniel A (2023) Development of low-resistance ohmic contacts with bilayer NiO/Al-doped ZnO thin films to p-type GaN. *ACS Appl Mater Interfaces* 15(6):8723–8729
- Tripathi R, Kumar A, Bharti C, Sinha TP (2010) Dielectric relaxation of ZnO nanostructure synthesized by soft chemical method. *Curr Appl Phys* 2:676–681
- Vinod Kumar OM, Ntwaeaborwa HCS (2020) Effect of oxygen partial pressure during pulsed laser deposition on the emission of Eu doped ZnO thin films. *Phys B* 576:411713
- Wang B-B, Feng J-T, Zhao Y-P, Yu TX (2010) Fabrication of novel superhydrophobic surfaces and water droplet bouncing

- behavior—Part 1: stable ZnO–PDMS superhydrophobic surface with low hysteresis constructed using ZnO nanoparticles. *J Adhes Sci Technol* 24(15–16):2693–2705
- Wenzel RN (1939) Resistance of solid surfaces to wetting by water. *Ind Eng Chem* 4
- Wu M, Chen WJ, Shen YH, Huang FZ, Li CH, Li SK (2014) In situ growth of matchlike ZnO/Au plasmonic heterostructure for enhanced photoelectrochemical water splitting. *ACS Appl Mater Interfaces* 6:15052–15060
- Wu-Qiang Wu, Lei B-X, Rao H-S, Yang-Fan Xu, Wang Y-F, Cheng-Yong Su, Kuang D-B (2013) Hydrothermal fabrication of hierarchically anatase TiO₂ nanowire arrays on FTO glass for dye-sensitized solar cells. *Sci Rep* 3:1352
- Young T (1805) An essay on the cohesion of fluids. *Philos Trans R Soc Lond* 95:65–87
- Zhang WD, Jiang LC, Ye JS (2009) Photoelectrochemical study on charge transfer properties of ZnO nanowires promoted by carbon nanotubes. *J Phys Chem C* 113:16247–16253
- Zhu XQ, Zhang JL, Chen F (2010) Hydrothermal synthesis of nanostructures Bi₂TiO₇ and their photocatalytic activity on acid orange 7 under visible light. *Chemosphere* 78:1350–1355
- Zhu S, Shan L, Chen X, He L, Chen J, Jiang M, Xie X, Zhou Z (2013) Hierarchical ZnO architectures consisting of nanorods and nanosheets prepared via a solution route for photovoltaic enhancement in dye-sensitized solar cells. *RSC Adv* 3:2910

Publisher's Note Springer Nature remains neutral with regard to jurisdictional claims in published maps and institutional affiliations.

Springer Nature or its licensor (e.g. a society or other partner) holds exclusive rights to this article under a publishing agreement with the author(s) or other rightsholder(s); author self-archiving of the accepted manuscript version of this article is solely governed by the terms of such publishing agreement and applicable law.